

# Modeling viscoplastic behavior and heterogeneous intracrystalline deformation of columnar ice polycrystals

R.A. Lebensohn<sup>a,\*</sup>, M. Montagnat<sup>b</sup>, P. Mansuy<sup>c</sup>, P. Duval<sup>b</sup>, J. Meysonnier<sup>b</sup>, A. Philip<sup>b</sup>

<sup>a</sup> Materials Science and Technology Division, Los Alamos National Laboratory, MS G755, Los Alamos, NM 87545, USA

<sup>b</sup> Laboratoire de Glaciologie et Géophysique de l'Environnement, CNRS, BP 96, 38402 St Martin d'Hères, France

<sup>c</sup> Centre de Technologies Michelin Ladoux, 63040 Clermont-Ferrand, France

Received 18 September 2008; received in revised form 23 October 2008; accepted 24 October 2008

Available online 2 January 2009

## Abstract

A full-field formulation based on fast Fourier transforms (FFT) has been adapted and used to predict the micromechanical fields that develop in two-dimensional columnar Ih ice polycrystals deforming in compression by dislocation creep. The predicted intragranular mechanical fields are in qualitative good agreement with experimental observations, in particular those involving the formation of shear and kink bands. These localized bands are associated with the large internal stresses that develop during creep in such anisotropic material, and their location, intensity, morphology and extension are found to depend strongly on the crystallographic orientation of the grains and on their interaction with neighboring crystals. The predictions of the model are also discussed in relation to the deformation of columnar sea and lake ice, as well as with the mechanical behavior of granular ice of glaciers and polar ice sheets.

Published by Elsevier Ltd. on behalf of Acta Materialia Inc.

**Keywords:** Ice; Creep; Microstructure; Shear bands; Micromechanical modeling

## 1. Introduction

Ih ice single crystals deform plastically in the dislocation glide regime essentially by  $(0001)\langle 1\bar{2}10 \rangle$  basal slip. The yield point observed during the early stage of plastic flow, associated with the formation of slip lines, is related to the multiplication of basal dislocations by slip, cross-slip and/or dislocation climb [1]. The stress required to produce a given effective strain-rate along a crystallographic direction not lying on the basal plane is between one and two orders of magnitude greater than the stress necessary to produce the same strain-rate along a direction belonging to the basal plane [2].

The single crystals that form glacier ice and polar ice sheets exhibit a wide range of sizes and morphologies, but, in general, the structure of this polycrystalline ice can be characterized as being “granular” or “three-dimen-

sional” (3-D). Another natural form of ice is the so-called “columnar” or “two-dimensional” (2-D) polycrystalline ice (also referred to as “S2” ice in glaciological literature [3]), consisting of an aggregate of columnar grains with the  $\langle c \rangle$ -axis of each single-crystal randomly oriented in the plane perpendicular to the direction of the columns. This kind of aggregate is obtained when ice grows from the surface of calm water in an unidirectional temperature gradient. This type of ice forms the natural covers of the Arctic Ocean and northern large rivers. Two-dimensional ice samples can be also prepared in the laboratory, for controlled testing [4–7].

The aforementioned very large viscoplastic anisotropy of ice single crystals has consequences on the mechanical response of ice polycrystals. On the one hand, the development of lattice preferred orientations (crystallographic textures) as ice deforms (e.g., when ice is transported into the depths of a polar ice sheet) determines the striking differences in the viscous response of textured ice polycrystals to stresses applied along different directions (e.g., [8]). On

\* Corresponding author.

E-mail address: [lebenso@lanl.gov](mailto:lebenso@lanl.gov) (R.A. Lebensohn).

the other hand, the fulfillment of both compatibility and stress equilibrium across grain boundaries results in heterogeneous intragranular deformation patterns [4–7,9–11]. High orientation gradients were observed in ice crystals extracted from the Antarctic ice sheet [12]. Dynamic continuous and discontinuous recrystallization, which is very active in ice sheets [13], contributes to the reduction of the long-range internal stresses field induced by such intragranular deformation heterogeneities.

Texture development in polar ice sheets and the resulting anisotropic response of polycrystalline ice have been intensively studied using mean-field models (e.g., [14–16]). This kind of approach is based on the statistical characterization of the intragranular mechanical fields (in terms of average grain stresses and strain-rates, and, in the most advanced formulations, also through the determination of the intracrystalline average field fluctuations [16]), but the actual micromechanical fields remain inaccessible to these homogenization approaches.

The modeling of the intracrystalline heterogeneity that develops in ice polycrystals (which requires the use of full-field approaches) has been, on the other hand, much less investigated. To fill this gap, this work is devoted to the study of the correlation existing between the heterogeneous deformation patterns that appear inside the constituent single-crystal grains of an ice aggregate and their corresponding crystallographic orientations, along with the influence of other factors, such as orientation and size of neighboring grains. To this end, a full-field formulation based on the fast Fourier transform (FFT) [17–19] has been adapted to obtain the micromechanical fields that develop in polycrystalline ice deforming by dislocation creep.

We have chosen to pursue this study on columnar ice polycrystals, for various reasons. On the one hand, dealing with a 2-D problem allowed us to use a higher resolution (i.e., more discretization points) to characterize the intracrystalline fields, and to fully visualize the results in a 2-D representation. Another advantage is that the mathematical representation of this kind of polycrystals is easier since each crystallographic orientation is almost fully characterized by only one angular parameter (rather than by three Euler angles, as in the case of 3-D polycrystals). Also, most importantly, we have available a comprehensive set of experimental results on crystal orientation and neighborhood type dependence of the intracrystalline localization patterns observed in laboratory grown and tested columnar ice specimens with different microstructures [4–7], which can be used for validation of our model predictions.

The plan of this paper is as follows. In Section 2 we review the available experimental evidence on the effective and local viscoplastic behavior of polycrystalline ice and recall some experimental results obtained by Mansuy [5] on the orientation- and microstructure-dependent deformation localization patterns in columnar ice polycrystals. In Section 3 we provide details of the model utilized and the unit cell used in this study. In Section 4 we present the results of our simulations and compare them with the

experimental evidence. In Section 5 we conclude discussing possible improvements of the modeling of natural polycrystalline ice, based on the capabilities of the present micromechanical formulation.

## 2. Mechanical behavior of polycrystalline ice

### 2.1. Effective and local viscoplastic behavior of polycrystalline ice

The secondary creep of polycrystalline ice is reached at strains of about 1%. The corresponding stress exponent is close to 3 for deviatoric stresses higher than 0.2 MPa [2]. Otherwise, for conditions prevailing in polar ice sheets (deviatoric stresses lower than 0.2 MPa and strain-rates lower than  $10^{-10} \text{ s}^{-1}$ ) the stress exponent for steady-state creep is lower than 2, as suggested by borehole deformation measurements [20], bubbly ice densification [21] and laboratory tests [22]. Under these very low stress and strain-rate conditions, dislocation creep remains the dominant deformation mode [23,24] but grain-boundary sliding [25,26] and grain-boundary migration [24] can also accommodate strain and control the deformation kinetics. Therefore, in what follows, for consistency with the assumption of dislocation glide being the exclusive viscoplastic deformation mechanism, and also for a meaningful comparison with laboratory measurements of deformation localization in columnar ice [4–7], obtained at strain-rates between  $10^{-8}$  and  $10^{-7} \text{ s}^{-1}$ , a stress exponent of 3 is assumed.

Hexagonal ice single crystals have a  $c/a$  relation of 1.629. Based on direct and indirect evidence (e.g., see Ref. [14] and references therein), it is usually assumed that they can deform by means of slip on three soft  $(0001)\{1\bar{2}10\}$  basal (“bas”) slip systems, three hard  $\{10\bar{1}0\}\{1\bar{2}10\}$  prismatic (“pr”) systems, and six hard  $\{11\bar{2}2\}\{11\bar{2}3\}$  pyramidal (“pyr”) systems. The rate-sensitive equation, relating the shear-rate on each slip system and the stress acting on the crystal, is given by

$$\dot{\gamma}^s = \dot{\gamma}_0 \left( \frac{m_{ij}^s \sigma'_{ij}}{\tau^s} \right)^n, \quad (1)$$

where  $\sigma'_{ij}$  is the deviatoric stress tensor,  $m_{ij}^s$  is the Schmid tensor of slip system ( $s$ ) defined as  $m_{ij}^s = (n_i^s b_j^s + n_j^s b_i^s)/2$ , with  $n^s$  and  $b^s$  being the normal and Burgers vectors of system ( $s$ );  $\dot{\gamma}^s$  and  $\tau^s$  are, respectively, the shear-rate and the threshold stress of slip system ( $s$ );  $n = 3$  is the creep exponent; and  $\dot{\gamma}_0$  is reference shear-rate. Hence, the single-crystal anisotropy is characterized by the ratio between the critical stresses of the different slip modes. In what follows, we have adopted  $\tau^{\text{pr}} = \tau^{\text{pyr}}$  and  $M = \tau^{\text{pr}}/\tau^{\text{bas}} = \tau^{\text{pyr}}/\tau^{\text{bas}}$ . The value of the anisotropic parameter  $M$  was adjusted to experiments, according to the following considerations. A normalized effective response of a viscoplastic material can be obtained in terms of the reference equivalent stress  $\sigma_0$ , defined as [14]:

$$\sigma_o = \left( \frac{\dot{\gamma}_o}{\dot{E}_{eq}} \right)^{1/n} \Sigma_{eq}, \quad (2)$$

where  $n$  is the macroscopic stress exponent, and  $\Sigma_{eq}$  and  $\dot{E}_{eq}$  are the macroscopic von Mises equivalent stress and strain-rate. For  $\dot{\gamma}_o = 1$ , a typical value of the reference stress for an isotropic ice polycrystal (i.e., one made of randomly oriented crystals), at  $-10$  °C, for a viscosity exponent  $n = 3$  is  $\sigma_o/\tau^{bas} = 18$  [14]. The latter relation expresses the ratio between the viscosity of a isotropic polycrystalline ice sample and a single-crystal deforming by basal glide. Previous studies [16] using the FFT-based model to calculate the effective response of isotropic ice showed a linear dependence of the reference stress  $\sigma_o$  with the anisotropy parameter  $M$ , with a slope very close to 1. Based on this scaling behavior, a value of the anisotropic parameter  $M = 20$  was adopted in the calculations that follow. It is worth noting that the choice of a higher  $M$  value does not change qualitatively the results to be presented below.

## 2.2. Deformation heterogeneity in columnar ice polycrystals

Mansuy [5,7] conducted a series of compression creep experiments at  $-10$  °C on laboratory-grown large columnar ice crystals and multicrystals with different orientations and surrounded by a matrix of smaller crystals. The specimens were plates of  $210 \times 140$  mm<sup>2</sup> with a relatively thick (8 mm) section, consisting of a large columnar single crystal or a multicrystalline cluster, located in the center of the plate, with columnar axes along plate thickness (i.e., having their  $\langle c \rangle$ -axes lying on the plane of the plate) and embedded in fine-grained ice matrices. In what follows, results of two types of specimens tested by Mansuy are going to be discussed and compared with corresponding simulations:

(a) Specimen #1 (Fig. 1), consisting of a single crystal with a circular section in the plane of the plate, measuring 30 mm in diameter, embedded in an isotropic matrix of very fine globular grains (of around 1 mm in diameter, i.e., small compared to the sample thickness) with random orientations. The  $\langle c \rangle$ -axis of the central crystal was inclined  $45^\circ$  with respect to the compression axis.

(b) Specimen #2 (Fig. 2), consisting of seven grains, hexagonal in shape, of about 20 mm in size, surrounded by a matrix of smaller (3–8 mm in diameter) columnar grains. The  $\langle c \rangle$ -axes of the central grains had different initial orientations in the plane of the plate.

These ice specimens were tested under compression exerted in the plane at  $-10$  °C. The applied compression stress was, respectively, 0.5 MPa for specimen #1 and 0.75 MPa for specimen #2. Fig. 1 shows the localization of the deformation in basal slip lines in specimen #1 after a strain of about 0.06. Fig. 2 shows, after about the same strain (0.07), three types of localization bands: basal shear bands, kink bands and sub-boundaries, that change orientation to follow crystallographic directions when they cross

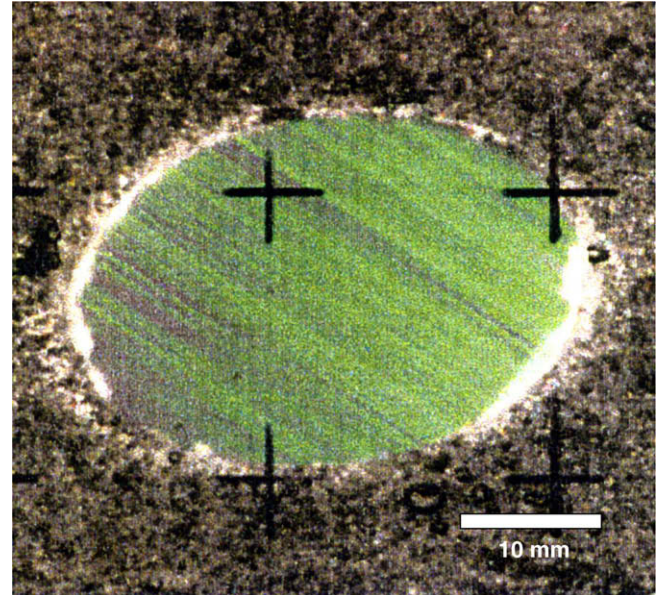


Fig. 1. Photograph of compression creep specimen #1 (after Mansuy [5]) between crossed polarizers, after a deformation of  $6.3 \times 10^{-2}$  at  $-10$  °C. The corresponding strain-rate was  $4.5 \times 10^{-8}$  s<sup>-1</sup>. The diameter of the initially circular monocrystalline inclusion was 30 mm. Parallel lines are the traces of the basal planes.

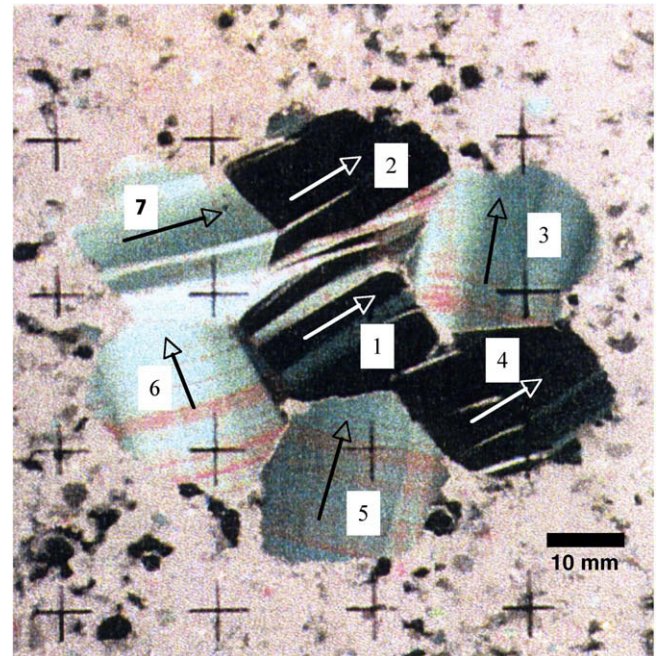


Fig. 2. Photograph of compression creep specimen #2 (after Mansuy [5]) between crossed polarizers, after a deformation of  $6.6 \times 10^{-2}$  at  $-10$  °C. The corresponding strain-rate was  $6.0 \times 10^{-8}$  s<sup>-1</sup>. The mean size of each hexagonal grain was 20 mm. Black and white arrows indicate the initial  $\langle c \rangle$ -axis orientations.

tation to follow crystallographic directions when they cross from one grain to another. Kink band boundaries are roughly parallel to the  $\langle c \rangle$ -axis and are seen inside grains well oriented for basal slip (grains #2 and #7). These kink

bands appear to form after some basal slip and the bending of basal planes [5,7]. On the other hand, kink bands are not observed in grains #3, #5 and #6, which are not well oriented for basal slip. Sub-boundaries parallel to the  $\langle c \rangle$ -axis can be seen in grain #3. The difference in behavior for the two types of specimens is related to the stress conditions at the interface between each crystal and its neighborhood. A better accommodation of basal slip by the fine-grained matrix explains the absence of shear and kink bands in the central grain of specimen #1.

It is worth noting that the formation of kink bands, described as a sharp or discontinuous change in orientation of the active slip surface, had been previously reported in many experimental studies conducted on 3-D ice polycrystals (e.g., [9–11]). In particular, Wilson et al. [10] reported the formation of kink bands in grains of a 3-D polycrystal deformed in plane-strain, with  $\langle c \rangle$ -axis lying on the plane containing the shortening and extension directions, normal to the shortening axis. Furthermore, kinking is not restricted to plastic deformation of ice. It has been reported to occur in different low-symmetry materials, both as an inelastic mechanism (alternative to easy glide and deformation twinning, when the former is not favorably oriented and the latter is inactive due to, for example, a high single crystal's  $c/a$  ratio [27–30]) and, recently, also as an elastic (reversible) deformation mechanism (e.g., [31,32]). Kink bands were also observed in face-centered cubic (fcc) single crystals (e.g., [33]), specially at sites of high stress concentration such as crack tips [34]. The development of these kink bands has been successfully simulated using crystal plasticity-based finite element (FE) analysis [34–36]. Therefore, the present analysis of the deformation of columnar polycrystalline ice can be regarded also as a model material study, to better understand this ubiquitous mechanism that kinking represents.

### 3. Model

#### 3.1. The FFT-based formulation

The intracrystalline states that develop during creep of polycrystalline ice can be obtained using an extension of an iterative method based on FFT, originally proposed by Moulinec and Suquet [17] and Michel et al. [18] for linear and nonlinear composites. This formulation was later adapted to polycrystals and applied to the prediction of texture development of fcc materials [19], and in turn used for the computation of field statistics and effective properties of power-law 2-D polycrystals [37,38] and 3-D cubic, hexagonal [39] and orthorhombic [40] materials. The FFT-based formulation was also recently applied to compute the development of local misorientations in polycrystalline copper, with direct input from orientation images [41]. The present work is the first application of this formulation for the prediction of local fields in non-cubic materials.

The FFT-based full-field formulation for viscoplastic polycrystals is conceived for a periodic unit cell, provides an exact solution of the governing equations, and has better numerical performance than a FE calculation for the same purpose and resolution. The viscoplastic FFT-based formulation consists in finding a strain-rate field, associated with a kinematically admissible velocity field, which minimizes the average of local work-rate, under the compatibility and equilibrium constraints. The method is based on the fact that the local mechanical response of a periodic heterogeneous medium can be calculated as a convolution integral between the Green function of a linear reference homogeneous medium and the actual heterogeneity field. This type of integral reduces to a simple product in Fourier space, and therefore the FFT algorithm can be used to transform the heterogeneity field into Fourier space and, in turn, to get the mechanical fields by antitransforming that product back to real space. However, since the actual heterogeneity field depends precisely on the a priori unknown mechanical fields, an iterative scheme should be implemented to obtain, upon convergence, a compatible strain-rate field and a stress field in equilibrium.

The periodic unit cell representing the polycrystal is discretized by means of a regular grid  $\{\mathbf{x}^d\}$ , which in turn determines a corresponding grid of the same dimensions in Fourier space  $\{\xi^d\}$ . Velocities and tractions along the boundary of the unit cell are left undetermined. An average velocity gradient  $V_{i,j}$  is imposed on the unit cell, which gives an average strain-rate  $\dot{E}_{ij} = \frac{1}{2}(V_{i,j} + V_{j,i})$ . The local strain-rate field is a function of the local velocity field, i.e.,  $\dot{\epsilon}_{ij}(v_k(\mathbf{x}))$ , and can be split into its average and a fluctuation term:  $\dot{\epsilon}_{ij}(v_k(\mathbf{x})) = \dot{E}_{ij} + \tilde{\epsilon}_{ij}(\tilde{v}_k(\mathbf{x}))$ , where  $v_i(\mathbf{x}) = \dot{E}_{ij}x_j + \tilde{v}_i(\mathbf{x})$ . By imposing periodic boundary conditions, the velocity fluctuation field  $\tilde{v}_k(\mathbf{x})$  is assumed to be periodic across the boundary of the unit cell, while the traction field is antiperiodic, to meet equilibrium on the boundary between contiguous unit cells. The local constitutive equation that relates the deviatoric stress  $\sigma'_{ij}(\mathbf{x})$  and the strain-rate  $\dot{\epsilon}_{ij}(\mathbf{x})$  at point  $\mathbf{x}$  is obtained from Eq. (1), adding the contribution of the 12 slip systems assumed to be active in the ice single crystal:

$$\begin{aligned} \dot{\epsilon}_{ij}(\mathbf{x}) &= \sum_{s=1}^{12} m_{ij}^s(\mathbf{x}) \dot{\gamma}^s(\mathbf{x}) \\ &= \dot{\gamma}_o \sum_{s=1}^{12} m_{ij}^s(\mathbf{x}) \left( \frac{m_{ij}^s(\mathbf{x}) \sigma'_{ij}(\mathbf{x})}{\tau^s(\mathbf{x})} \right)^3. \end{aligned} \quad (3)$$

If  $p(\mathbf{x})$  is the hydrostatic pressure field, the Cauchy stress field can be written as:

$$\sigma_{ij}(\mathbf{x}) = L_{ijkl}^o \dot{\epsilon}_{kl}(\mathbf{x}) + \varphi_{ij}(\mathbf{x}) - p(\mathbf{x}) \delta_{ij}, \quad (4)$$

where the polarization field  $\varphi_{ij}(\mathbf{x})$  is given by

$$\varphi_{ij}(\mathbf{x}) = \sigma'_{ij}(\mathbf{x}) - L_{ijkl}^o \dot{\epsilon}_{kl}(\mathbf{x}), \quad (5)$$

and where  $L^o$  is the stiffness of a linear reference medium. Combining Eq. (5) with the equilibrium and the incompressibility conditions gives

$$\begin{cases} L_{ijkl}^o v_{k,lj}(\mathbf{x}) + \varphi_{ij,j}(\mathbf{x}) - p_{,i}(\mathbf{x}) = 0, \\ v_{k,k}(\mathbf{x}) = 0. \end{cases} \quad (6)$$

The system of differential equations (5), with periodic boundary conditions across the unit cell boundary, can be solved by means of the Green function method. If  $G_{km}$  and  $H_m$  are the periodic Green functions associated with the velocity and hydrostatic pressure fields, the solutions of system (6) are convolution integrals between those Green functions and the actual polarization term. In the case of the velocity and its gradient, after some manipulation:

$$\tilde{v}_k(\mathbf{x}) = \int_{R^3} G_{ki,j}(\mathbf{x} - \mathbf{x}') \varphi_{ij}(\mathbf{x}') d\mathbf{x}', \quad (7)$$

$$\tilde{v}_{i,j}(\mathbf{x}) = \int_{R^3} G_{ik,jl}(\mathbf{x} - \mathbf{x}') \varphi_{kl}(\mathbf{x}') d\mathbf{x}'. \quad (8)$$

Convolution integrals in direct space are simply products in Fourier space. Hence

$$\hat{\tilde{v}}_k(\boldsymbol{\xi}) = (-i\xi_j) \hat{G}_{ki}(\boldsymbol{\xi}) \hat{\varphi}_{ij}(\boldsymbol{\xi}), \quad (9)$$

$$\hat{\tilde{v}}_{i,j}(\boldsymbol{\xi}) = \hat{\Gamma}_{ijkl}^{\text{sym}}(\boldsymbol{\xi}) \hat{\varphi}_{kl}(\boldsymbol{\xi}), \quad (10)$$

where  $\Gamma_{ijkl}^{\text{sym}} = \text{sym}(G_{ik,jl})$ . The tensors  $\hat{G}_{ij}(\boldsymbol{\xi})$  and  $\hat{\Gamma}_{ijkl}^{\text{sym}}(\boldsymbol{\xi})$  are only functions of  $L^o$  and can be readily obtained for every point belonging to  $\{\boldsymbol{\xi}^d\}$  (for details, see Ref. [41]). Having current estimates of the strain-rate field in the regular grid  $\{\mathbf{x}^d\}$  and computing the corresponding stress field from the local constitutive relation (Eq. (3)) allows us to obtain a guess for the polarization field in direct space  $\varphi_{ij}(\mathbf{x}^d)$  (Eq. (5)), from which, by application of FFT,  $\hat{\varphi}_{ij}(\boldsymbol{\xi}^d)$  can be readily calculated. An improved guess for the strain-rate field in  $\{\mathbf{x}^d\}$  can be then obtained antitransforming Eq. (10), and so on. The actual iterative procedure used in the present case of creep of polycrystalline ice is based on an augmented Lagrangian algorithm [17] that guarantees that the converged stress and strain-rate fields fulfill equilibrium and compatibility, respectively (see Refs. [18,41] for details).

Upon convergence, the stress at each material point can be used to calculate the shear-rates associated with each slip system (Eq. (1)), from which fields of relative activity of the basal, prismatic and pyramidal slip modes can be obtained as well.

It is worth noting that, while it is certainly possible to use the present FFT-based formulation for the prediction of microstructure evolution (e.g., using an explicit scheme such that the strain-rate and velocity fields, and the corresponding local lattice rotation-rates [41] are assumed constant during a time interval, and thus can be integrated to predict local texture evolution, morphological changes of the grains and local strain-hardening), in this work, we have restricted our analysis to the local fields that are obtained for a fixed configuration. In this sense, for example, the high strain-rate regions predicted by the model (see below) should be regarded as precursors of localization bands. Evidently, microstructural changes that are not con-

sidered under this approximation, such as the eventual grains' and subgrains' morphological evolution and rotation, as well as the possible occurrence of local strain-hardening (although the latter remains small in ice deforming at high temperature), may modify some of the trends observed in the initial micromechanical fields. In order to account for these microstructural changes, we are presently in the process of coupling the FFT-based formulation with a front-tracking numerical platform [42]. Results of this coupled model will be reported elsewhere [43,44].

### 3.2. Unit cell construction

The crystallographic texture of a 2-D ice polycrystal consisting of columnar grains with  $\langle c \rangle$ -axes perpendicular to the axial (vertical) direction  $x_3$  can be described in terms of a collection of Euler angles triplets of the form  $(\varphi_1, 90^\circ, \varphi_2)$  (Bunge convention). The angle  $\varphi_1$  determines the orientation of the  $\langle c \rangle$ -axis on the plane perpendicular to the columnar direction and  $\varphi_2$  gives the rotation of the hexagonal prism (i.e., the conventional unit cell of the hexagonal close-packed (hcp) crystal structure) around its  $\langle c \rangle$ -axis. The application of the FFT method required the generation of a periodic unit cell or representative volume element (RVE), by repetition along  $x_1$  and  $x_2$  of a square domain. This square domain was constructed in such a way that it contained the cross-sections of 200 columnar grains, generated by Voronoi tessellation (see Fig. 3). Each Voronoi partition represents the cross-section of a columnar grain with orientation  $(\varphi_1, 90^\circ, \varphi_2)$ , where  $\varphi_1$  and  $\varphi_2$  were randomly selected from the interval  $[-180^\circ, 180^\circ]$

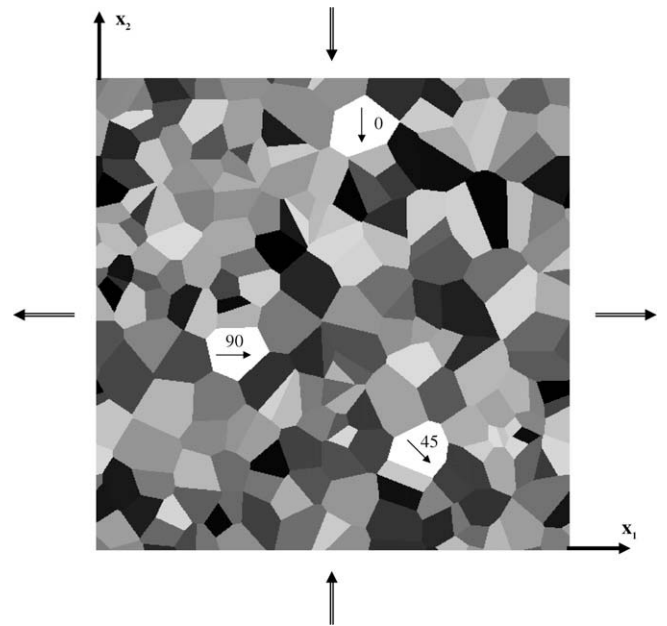


Fig. 3. Unit cell containing the cross-sections of 200 columnar grains generated by Voronoi tessellation. The three hand-picked orientations:  $(0^\circ, 90^\circ, 0^\circ)$ ,  $(45^\circ, 90^\circ, 0^\circ)$  and  $(90^\circ, 90^\circ, 0^\circ)$ , and the extension and shorting directions are also indicated.

(except for three grains assigned with hand-picked orientations, see below). This square domain is the cross-section of the unit cell, consisting of columnar grains with axes along  $x_3$  and sections in the  $x_1$ – $x_2$  plane. This unit cell was discretized using a  $1024 \times 1024 \times 1$  grid of regularly spaced Fourier points, resulting in an average of around 5250 Fourier points per grain. Note that the periodic repetition of this unit cell along  $x_3$  determines infinitely long grains along this direction.

For reasons that will become apparent below, the following three orientations:  $(0^\circ, 90^\circ, 0^\circ)$ ,  $(45^\circ, 90^\circ, 0^\circ)$ ,  $(90^\circ, 90^\circ, 0^\circ)$  were forced to make part of the set of 200 (otherwise random) orientations assigned to the grains. For this, three relatively big Voronoi cells with large separations between each other (located in the lower left, at the center, and in the upper right sections of the unit cell, see Fig. 3), were, respectively, designated to have the above orientations. In Fig. 3, the arrows indicate the orientation of the corresponding  $\langle c \rangle$ -axes. For a plane-strain state, such that  $x_1$  is the tensile direction and  $x_2$  is the compression direction, the grain with  $\varphi_1 = 45^\circ$  (“45°” grain in what follows) is favorably oriented to deform by soft basal slip, while in the “0°” and “90°” grains, the hard pyramidal systems are the only ones favorably oriented to accommodate deformation. It is worth noting that due to the above plane-strain condition and the in-plane orientation of the  $\langle c \rangle$ -axes, the prismatic slip systems are not well oriented, for any  $\varphi_1$  angle.

#### 4. Results and discussion

A FFT-based calculation was run to obtain the overall and local mechanical response of the above-described unit cell representing a columnar ice polycrystal, to the following imposed strain-rate tensor (see also Fig. 3):

$$\dot{E}_{ij} = \begin{bmatrix} 1 \times 10^{-8} & 0 & 0 \\ 0 & -1 \times 10^{-8} & 0 \\ 0 & 0 & 0 \end{bmatrix} \text{ s}^{-1}. \quad (11)$$

The computed effective equivalent stress reached a value of 0.01875 in units of  $\tau^{\text{bas}}$ , resulting in a normalized reference equivalent stress  $\sigma_o$  (see Eq. (2)) [14] of  $9.11 \times \tau^{\text{bas}}$ . This roughly represents an effective response twice as soft for this kind of isotropic columnar ice polycrystal deformed in-plane, compared to an isotropic 3-D polycrystalline ice (the magnitude of  $\sigma_o$  of the latter, in units of  $\tau^{\text{bas}}$ , is around the value of the single crystal’s anisotropic parameter [16], i.e.,  $\sigma_o \cong 20 \times \tau^{\text{bas}}$  in the present case). As expected, the computed overall relative activities of the different slip modes (i.e., 90.7%, 7.6% and 1.7% for basal, pyramidal and prismatic slip, respectively) show a pre-eminence of basal slip, a minor contribution of pyramidal slip and a very low activity of prismatic slip.

Fig. 4 shows the computed equivalent strain-rate field for the entire unit cell, normalized with respect to the average equivalent strain-rate ( $\dot{E}_{\text{eq}} = 1.15 \times 10^{-8} \text{ s}^{-1}$ ). The

main feature observed in this plot is a network of high strain-rate bands, precursors of localization bands (in what follows we will sometimes refer to them simply as “localization bands”). These bands are transmitted from grain to grain, and are, in general, inclined with respect to the shortening and extension directions. They follow tortuous paths, sometimes with large deviations from  $45^\circ$  (i.e., the macroscopic directions of maximum shear stress). As will be shown in more detail below, the reason for this is that they follow crystallographic directions (basal poles or basal planes) inside each grain. Note that, since the existing experimental evidence [5,10] shows an excellent correlation between the orientation of the band with respect to the crystallographic  $\langle c \rangle$ -axis and its shear- or kink-band character (the latter having been actually determined by basal slip trace analysis), and since the only information extractable from our continuum modeling approach is the orientation of the band with respect to crystallographic directions, the predicted bands parallel or perpendicular to the  $\langle c \rangle$ -axis will be reasonably assumed to be kink or shear bands, respectively. Some segments of these bands also follow favorably oriented grain boundaries and frequently go through triple or multiple points between grains, in good agreement with some of Mansuy’s [5] observations (see Fig. 2). These transgranular bands usually fade and eventually stop inside grains whose orientations force the bands to adopt an orientation close to  $0^\circ$  or  $90^\circ$ . The most intense bands ( $>10$  times the macro strain-rate) are thinner and generally only one of them is found inside a given grain. Less intense bands appear in parallel pairs inside some grains, connected by another system of orthogonal and even less intense bands (see also field predictions in the vicinity of the  $45^\circ$  grain below).

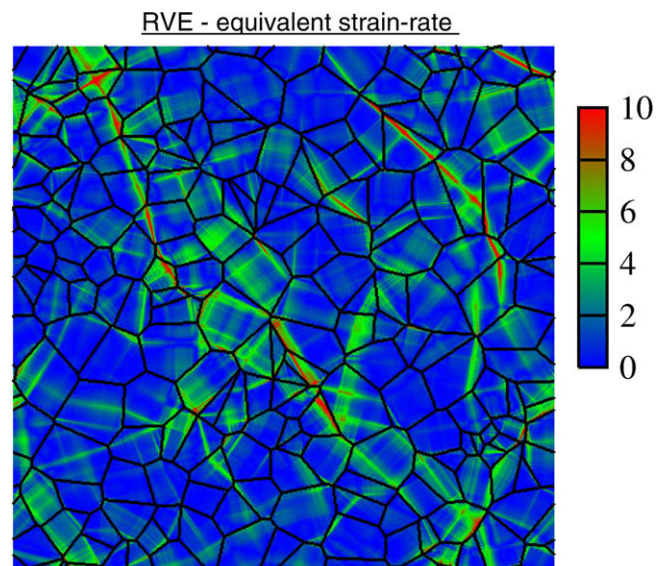


Fig. 4. Predicted equivalent strain-rate field over the entire unit cell of Fig. 1, normalized with respect to the average equivalent strain-rate ( $\dot{E}_{\text{eq}} = 1.15 \times 10^{-8} \text{ s}^{-1}$ ).

The next three figures show in more detail the predicted fields of equivalent strain-rate (normalized to  $\dot{E}_{eq}$ ), equivalent stress (in units of  $\tau^{bas}$ ) and relative basal activity, in the vicinities of the  $0^\circ$ ,  $45^\circ$  and  $90^\circ$  grains, together with the map of randomly assigned orientations of the surrounding grains in those vicinities. Fig. 5 corresponds to the vicinity of the  $45^\circ$  grain. Two very intense (i.e., local strain-rates higher than 10 times the macroscopic strain-rate) and parallel kink bands (note the alignment of the latter with the basal pole direction) are seen inside the  $45^\circ$  grain, connected by several less intense shear bands (orthogonal to the pair of kink bands, lying on to the basal plane), in good agreement with Mansuy's experiments (see Fig. 2). Both bands go through triple and quadruple points formed by the central grain and neighbor crystals. The upper kink band propagates down and to the right, into the  $-54.9^\circ$  grain, in the form of a shear band. The lower band propagates up and to the left, following two well oriented (i.e., with an inclination close to  $45^\circ$ ) grain boundaries. The basal activity in the  $45^\circ$  grain is very high, although some regions of higher non-basal activity can be observed between shear bands and immediately outside the kink bands. The latter is compatible with a low or even vanishing resolved shear stress on basal planes in those locations,

which may be responsible for the formation of basal dislocation walls that are at the origin of a kink band [5,7]. This correlation between kink band precursors and nearby localized higher non-basal activity is systematic in our results.

In the case of the surroundings of the  $0^\circ$  grain (Fig. 6) one can observe a shear band coming into the central grain, out of the highly stressed quadruple point on the right that struggles to propagate inside the  $0^\circ$  grain. The only clear kink band is found in the  $37.2^\circ$  crystal, again well oriented for basal slip. No kink band precursors are observed in the  $0^\circ$  grain. This is compatible with the absence of a clear indication of kink bands in grains #5 and #6 of Fig. 2. The reason for this behavior is that kink bands in grains of such orientation are ineffective at accommodating the applied deformation (i.e., shortening along the compressive direction or extending along the tensile direction).

The  $90^\circ$  grain and its vicinity are shown in Fig. 7. Localization bands near grain boundaries are found in the  $155.9^\circ$  and  $-53.1^\circ$  grains. A kink region initiates at a triple point between the central grain and the  $82.9^\circ$  and  $58.0^\circ$  crystals, by the confluence of two bands coming from these neighbors, but it vanishes inside the grain. It is also worth noting that the sharp shear band observed in grains with a small

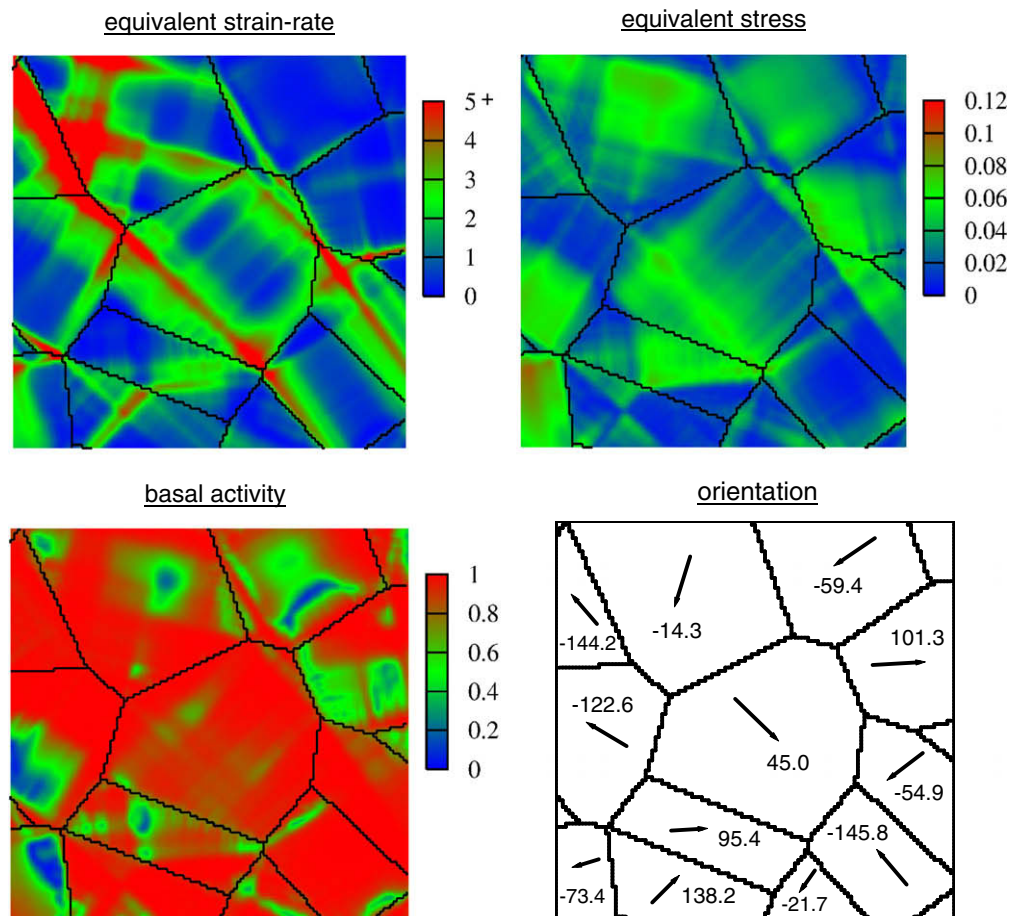


Fig. 5. Predicted fields of equivalent strain-rate (normalized to  $\dot{E}_{eq}$ ), equivalent stress (in units of  $\tau^{bas}$ ), relative basal activity, and map of neighboring orientations, for the  $45^\circ$  grain and its surroundings.

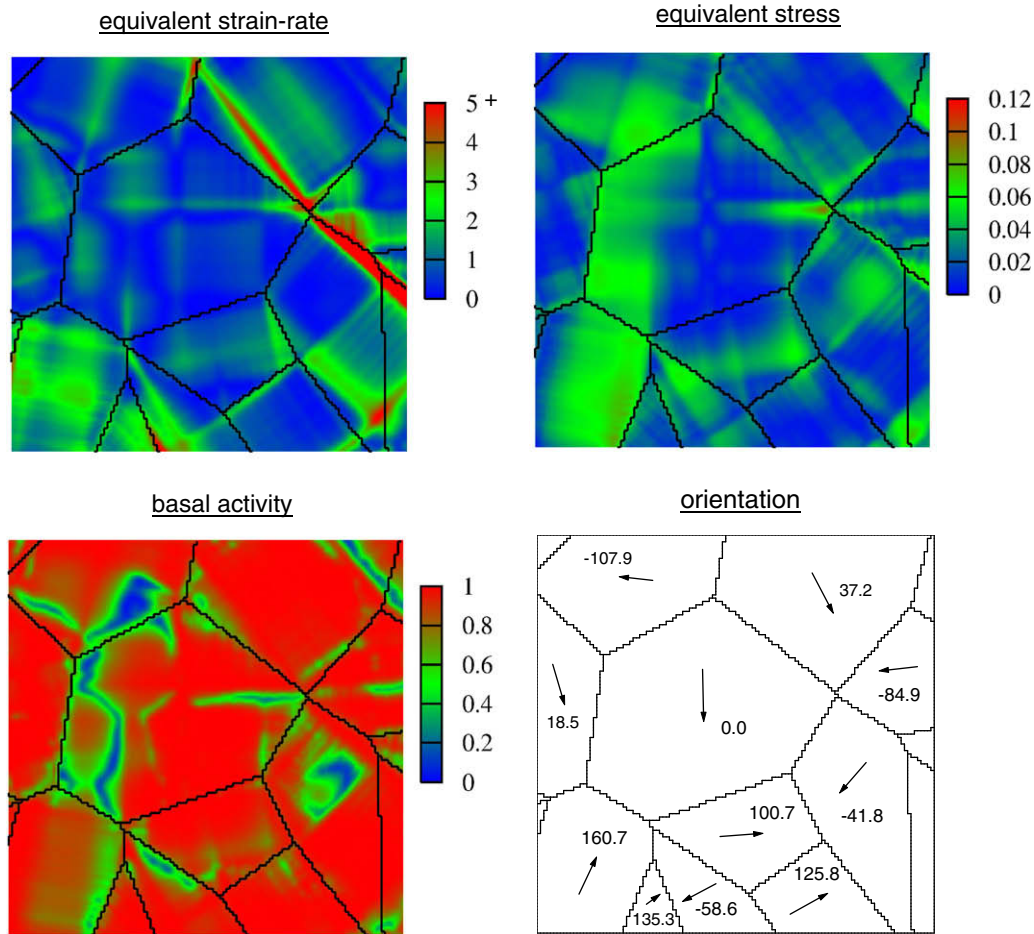


Fig. 6. Predicted fields of equivalent strain-rate (normalized to  $\dot{E}_{eq}$ ), equivalent stress (in units of  $\tau^{bas}$ ), relative basal activity, and map of neighboring orientations, for the  $0^\circ$  grain and its surroundings.

tilt with respect to  $90^\circ$ , such as the  $82.9^\circ$  grain on the upper left, indicates the possibility of finding intense basal slip lines in grains with orientations very close to  $90^\circ$ , as also reported by Mansuy [5]. In such grains, a relatively low basal activity and a relatively high equivalent stress is observed.

The effect of the size of the surrounding crystals on the deformation heterogeneity of large grains is analyzed next. Fig. 8 shows another RVE configuration studied using the FFT-based approach. This unit cell was constructed as follows. A new 2-D Voronoi tessellation with 100,000 grains was generated and discretized using the same number of Fourier points ( $1024 \times 1024$ ) as before. The resulting average grain size (linear dimensions, in the same units as the distance between two adjacent Fourier points) is given by

$$d = \sqrt{(1024)^2/100,000} \approx 3. \text{ Since the average grain size}$$

of the original RVE was  $\sqrt{(1024)^2/200} \approx 72$ , the ratio between these two average grain sizes roughly represents the ratio between the linear dimensions of the large central single crystal and the surrounding globular grains of Mansuy's specimen #1 shown in Fig. 1. Next, the two Voronoi structures (i.e., of 200 and 100,000 grains, respectively)

were superimposed and combined. In this combination, the small grains were kept, except for the  $0^\circ$ ,  $45^\circ$  and  $90^\circ$  grains, which replaced the overlapping fine grains, resulting in the configuration of Fig. 8. The predicted equivalent strain-rate field is shown in Fig. 9. While the  $0^\circ$  and  $90^\circ$  grains deform very little, the strain-rate field inside the  $45^\circ$  grain is around two times the average strain-rate, with much less fluctuation than in the RVE surrounded by large grains. However, unlike Mansuy's specimen #1 (see Fig. 1), both types of (mild) bands of higher strain-rate (contained in, and perpendicular to, the basal plane, respectively) were predicted. The retained sharp angles of the  $45^\circ$  grain (as opposite to the circular geometry of the central crystal of Fig. 1) are the likely cause of this disagreement. In any case, our model clearly predicts that localization in large grains is likely to be prevented (or at least delayed) as the grain size of the surrounding crystals decreases.

In what concerns the strain-rate field predicted in the matrix outside the large grains, it is apparent from the comparison of Figs. 4 and 9 that the length of the localization bands correlates with the typical grain size of the microstructure. This result of our model can be qualitatively compared with Doumalin et al.'s observations [45,46] on

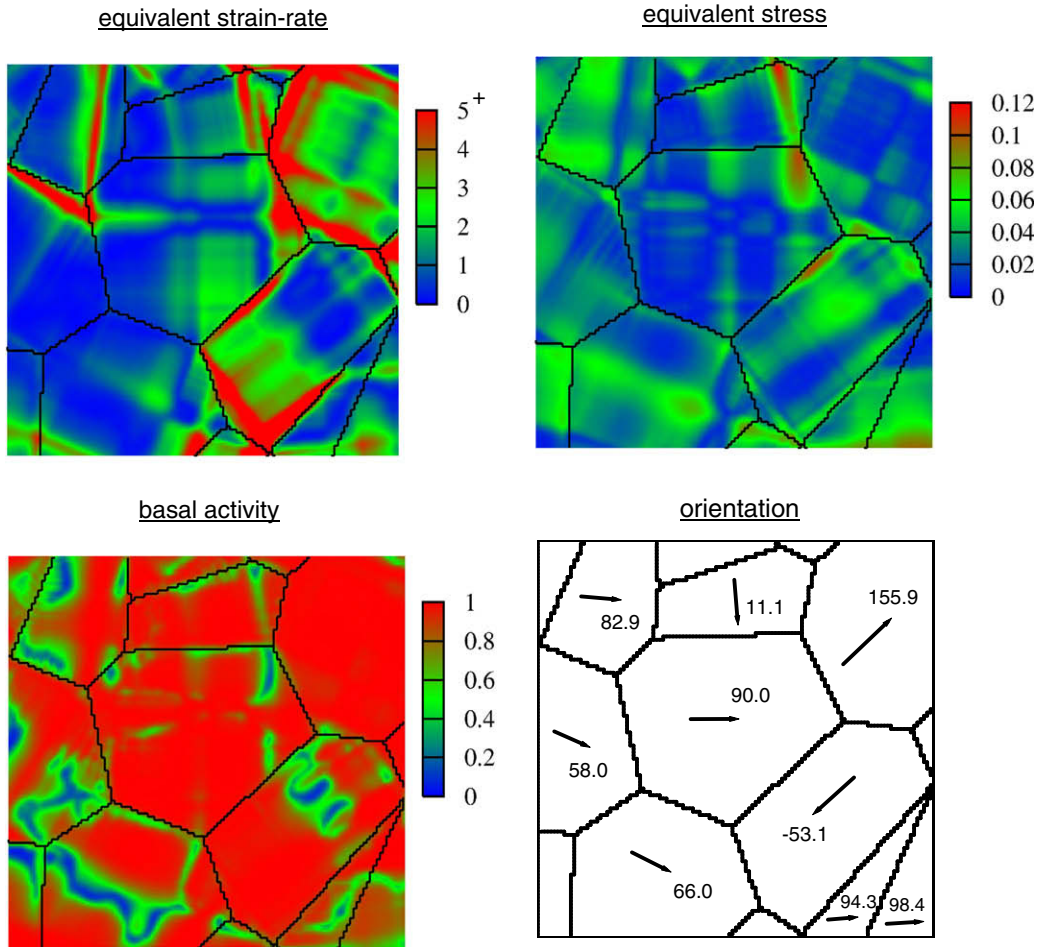


Fig. 7. Predicted fields of equivalent strain-rate (normalized to  $\dot{E}_{eq}$ ), equivalent stress (in units of  $\tau^{bas}$ ), relative basal activity, and map of neighbor orientations, for the  $90^\circ$  grain and its surroundings.

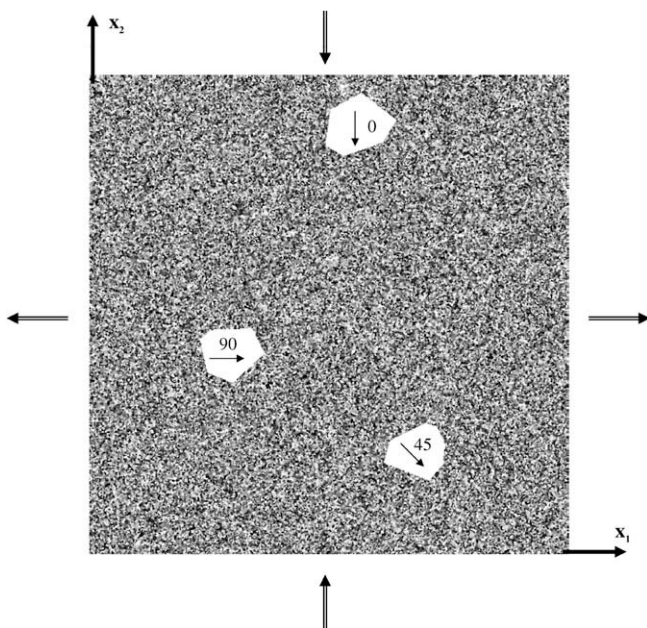


Fig. 8. Unit cell obtained combining 100,000 Voronoi grains and the three grains of the 200 grain unit cell of Fig. 1 with hand-picked orientations.

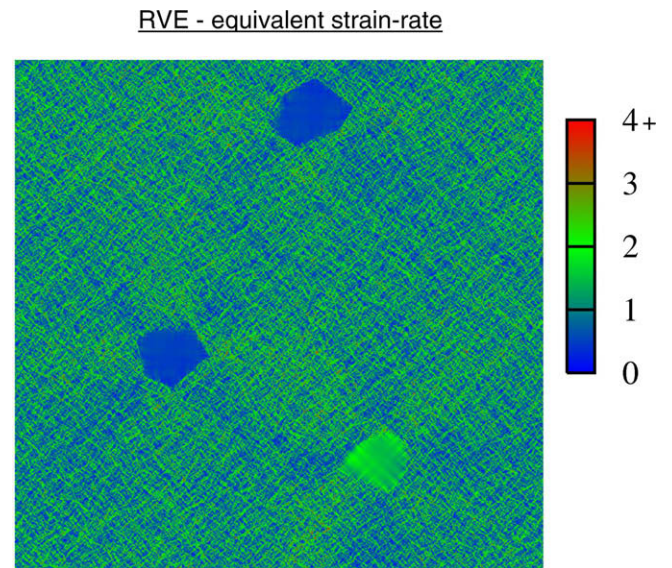


Fig. 9. Predicted equivalent strain-rate field over the entire unit cell of Fig. 8, normalized with respect to the average equivalent strain-rate ( $\dot{E}_{eq} = 1.15 \times 10^{-8} \text{ s}^{-1}$ ).

strain localization patterns in different heterogeneous materials. These authors have used microextensometry techniques to characterize strain localization bands in a Ni/Ag two-phase material deformed plastically in compression, forming at  $\pm 45^\circ$  with respect to the compression axis, and having a characteristic length of between two and six times the correlation length of the phase distribution [45]. Also, in polycrystalline Zr deformed in tension, localization bands were formed at a slightly higher angle ( $\pm 52^\circ$ ) with respect to the tensile direction, with a characteristic length of 5–10 times the aggregate's grain size [46]. Although the precise value of the factor between the length of the localization bands and the heterogeneity length-scale evidently depends on the mechanical contrast between phases, or on the single-crystal anisotropy, our simulations are in good qualitative agreement with Doumalin et al.'s observations. This can be seen in Fig. 10, which shows the strain-rate field (in two different scales, and with and without grain boundaries superimposed) in the neighborhood of the  $45^\circ$  grain.

## 5. Concluding remarks

A full-field formulation was adapted and used to predict the micromechanical fields that develop in columnar ice polycrystals deformed under plane-strain compression. This formulation, conceived as a very efficient alternative to FE methods (which calculation times usually scale with  $N^2$ , where  $N$  is the number of discretization points), is based on the repetitive use of the FFT algorithm, whose computing time scales with  $N \times \log N$ . This high numerical efficiency combined with the resolution of the 2-D problem associated with the deformation of columnar ice polycrystals allowed us to obtain very detailed predictions of the intragranular mechanical fields.

Under the assumption of creep deformation accommodated exclusively by dislocation glide (consistent with stresses  $> 0.3$  MPa and strain-rates  $> 10^{-8} \text{ s}^{-1}$ ), the deformation

heterogeneity predicted by the model is in good qualitative agreement with the available experimental evidence. Narrow regions of high strain-rate comprising several grains, compatible with the subsequent formation of localization bands lying on the basal plane (shear bands) and perpendicular to the basal plane (kink bands), were found, and their dependence with crystallographic orientation, grain morphology and interaction with neighboring grains was studied and validated. In the laboratory, kink bands were observed to form after significant basal slip [5,10] and, especially, in grains well oriented for basal slip (Fig. 2). From Figs. 6 and 7, kink bands predicted by the FFT model were also not observed in the  $0^\circ$  and  $90^\circ$  grains, which are not well oriented for basal slip. Kink bands with basal planes parallel to the compression axis have been observed in 2-D columnar ice, but at a strain-rate of about  $10^{-5} \text{ s}^{-1}$ , within the ductile–brittle transition [47]. At these high strain-rates, cracks induced by the pile-up of dislocations were observed at the kink band boundaries. It is worth noting that the difficulty of initiating reversible incipient kink bands in ice, which are seen to nucleate on the easy slip plane in several anisotropic hexagonal metals when loaded parallel to this plane [30–32], is related to the brittle behavior of ice at relatively low stresses [48,49].

Kink bands, as predicted by the FFT-based model, are expected to form easily in 2-D columnar sea and lake ice [9], especially in high pressure zones located at the interface between ice and rigid marine structures. On the other hand, this is generally not the case in 3-D natural glacier ice that deforms at strain-rates generally lower than  $10^{-9} \text{ s}^{-1}$ . At those low stresses and strain-rates, alternative accommodation processes, such as grain growth, dynamic recrystallization and, possibly, diffusion and grain-boundary sliding can efficiently contribute to reduce the long-range internal stress field associated with the mismatch of slip at grain boundaries in such anisotropic material. These accommodation processes should therefore preclude the formation of kink bands [10]. This may be the reason why kink bands

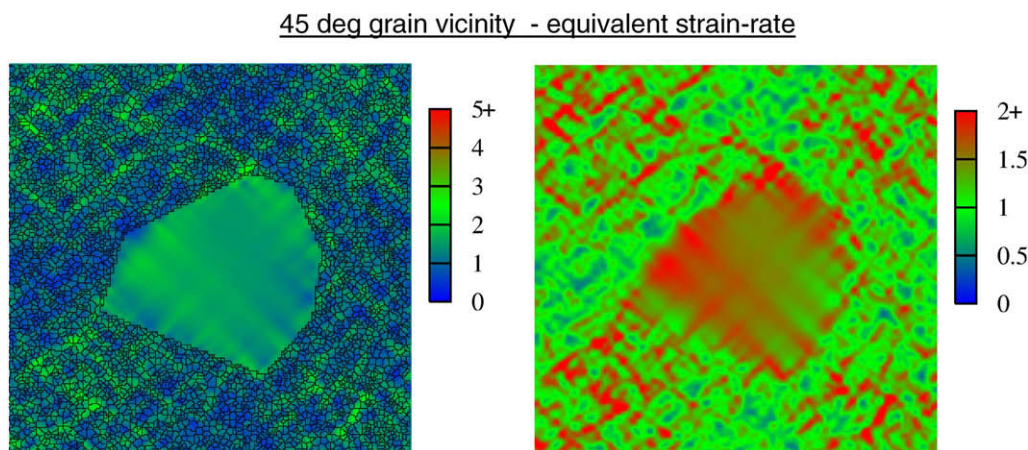


Fig. 10. Predicted equivalent strain-rate field corresponding to the unit cell of Fig. 8 in the vicinity of the  $45^\circ$  grain, normalized with respect to the average equivalent strain-rate ( $\dot{\epsilon}_{\text{eq}} = 1.15 \times 10^{-8} \text{ s}^{-1}$ ). Left column: Grain boundaries shown and highest color in the scale represents intensities of 5+. Right column: Highest color in the scale represents intensities of 2+ and grain boundaries are not plotted.

have never been observed in polar ice sheets. On the other hand, the active slip modes in 2-D and 3-D ices can be different. In the present FFT-based simulations, the predicted relative activity of non-basal slip was less than 10%, and essentially associated with pyramidal slip. The rather low activity of the prismatic slip systems (1.7%), compared with that predicted for a 3-D granular ice (about 8%) [14] is related to a vanishing resolved component of the applied stress on the prismatic planes when 2-D ice is deformed under compression normal to the columnar axis.

The present micromechanical formulation can be adapted to 3-D granular ice and used as a basis to account for more of the relevant accommodation processes taking place in polar ice sheets, but it obviously needs further improvement. Microstructural update using an explicit scheme as explained at the end Section 3.1 can provide information about the development of dislocation structures. Intragranular misorientations [41] and the excess dislocation density fields [50] can be readily obtained and incrementally updated by numerical derivation of the predicted deformation gradient field. In turn, these fields, in combination with an appropriate thermomechanical modeling platform (e.g., [42]), can be used to calculate local driving forces for the prediction of dynamic recrystallization [43,44]. Furthermore, a more straightforward and quantitative comparison with experimental evidence can be achieved using the present model in combination with direct input from microstructure images, integrating in situ electron backscattering diffraction observations (e.g., [51,52] in the specific case of ice polycrystals) with numerical simulations [51].

## Acknowledgments

This work was partially supported by the Office of Basic Energy Sciences, Project FWP 06SCPE401 (USA), and by CNRS (ST2I Department) and University Joseph Fourier, Grenoble (France).

## References

- [1] Montagnat M, Weiss J, Chevy J, Duval P, Brunjail H, Bastie P, et al. *Philos Mag* 2006;86:4259.
- [2] Duval P, Ashby MF, Anderman I. *J Phys Chem* 1983;87:4066.
- [3] Michel B, Ramseier RO. *Can Geotech J* 1971;8:36.
- [4] Mansuy P, Philip A, Meyssonier J. *Ann Glaciol* 2000;30:121.
- [5] Mansuy P. Contribution à l'étude du comportement viscoplastique d'un multicristal de glace: hétérogénéité de la déformation et localisation, expériences et modèles. Grenoble, France: Thèse de l'Université Joseph Fourier; 2001.
- [6] Mansuy P, Philip A, Meyssonier J. *J Phys IV* 2001;11:267.
- [7] Mansuy P, Meyssonier J, Philip A. *Comput Mater Sci* 2002;25:142.
- [8] Pimienta P, Duval P, Lipenkov VY. Constitutive properties of ice at Dye 3, Greenland. Physical basis of ice sheet modelling. Vancouver: AIHS; 1987. p. 57.
- [9] Gold LW. Deformation mechanisms in ice. In: Kingery WD, editor. *Ice and snow*. Cambridge (MA): MIT Press; 1963. p. 8.
- [10] Wilson CJL, Burg JP, Mitchell JC. *Tectonophysics* 1986;127:27.
- [11] Wilson CJL, Zhang Y. *J Glaciol* 1994;40:46.
- [12] Montagnat M, Duval P, Bastie P, Hamelin B, Lipenkov VY. *Earth Planet Sci Lett* 2003;214:369.
- [13] De La Chapelle S, Castelnau O, Lipenkov VY, Duval P. *J Geophys Res B* 1998;103:5091.
- [14] Castelnau O, Duval P, Lebensohn RA, Canova GR. *J Geophys Res B* 1996;101:13851.
- [15] Castelnau O, Canova GR, Lebensohn RA, Duval P. *Acta Mater* 1997;45:4823.
- [16] Lebensohn RA, Tomé CN, Ponte Castañeda P. *Philos Mag* 2007;87:4287.
- [17] Moulinec H, Suquet P. *Comput Methods Appl Mech Eng* 1998;157:69.
- [18] Michel JC, Moulinec H, Suquet P. *Comput Model Eng Sci* 2000;1:79.
- [19] Lebensohn RA. *Acta Mater* 2001;49:2723.
- [20] Dahl-Jensen D, Gundestrup NS. Constitutive properties of ice at Dye 3, Greenland. Physical basis of ice sheet modelling. Vancouver: AIHS; 1987. p. 31.
- [21] Lipenkov VY, Salamatin A, Duval P. *J Glaciol* 1997;43:397.
- [22] Montagnat M, Duval P. *CR Phys* 2004;5:699.
- [23] Alley RB. *J Glaciol* 1992;38:245.
- [24] Montagnat M, Duval P. *Earth Planet Sci Lett* 2000;183:179.
- [25] Goldsby DL, Kohlstedt DL. *Scr Mater* 1997;37:1399.
- [26] Goldsby DL, Kohlstedt DL. *J Geophys Res B* 2001;106:11017.
- [27] Orowan E. *Nature (London)* 1942;149:643.
- [28] Hess JB, Barrett CS. *Trans AIME* 1949;185:599.
- [29] Farber L, Levin I, Barsoum MW. *Philos Mag Lett* 1999;79:163.
- [30] Barsoum MW, Farber L, El-Raghy T. *Metall Mater Trans A* 1999;30:1727.
- [31] Barsoum MW, Zhen T, Kalidindi SR, Radovic M, Murugaiah A. *Nat Mater* 2003;2:107.
- [32] Barsoum MW, Zhen T, Zhou A, Basu S, Kalidindi SR. *Phys Rev B* 2005;71:134101.
- [33] Mader S, Seeger A. *Acta Metall* 1960;8:513.
- [34] Flouriot S, Forest S, Cailletaud G, Koster A, Remy L, Burgardt B, et al. *Int J Fracture* 2003;124:43.
- [35] Forest S. *Acta Mater* 1998;46:3265.
- [36] Forest S, Boubidi P, Sievert R. *Scr Mater* 2001;44:953.
- [37] Lebensohn RA, Liu Y, Ponte Castañeda P. *Proc R Soc Lond A* 2004;460:1381.
- [38] Lebensohn RA, Castelnau O, Brenner R, Gilormini P. *Int J Solids Struct* 2005;42:5441.
- [39] Lebensohn RA, Liu Y, Ponte Castañeda P. *Acta Mater* 2004;52:5347.
- [40] Castelnau O, Blackman DK, Lebensohn RA, Ponte Castañeda P. *J Geophys Res B* 2008;113:B09202.
- [41] Lebensohn RA, Brenner R, Castelnau O, Rollett AD. *Acta Mater* 2008;56:3914.
- [42] Jessell MW, Bons PD, Evans L, Barr TD, Stuwe K. *Comput Geosci* 2001;27:17.
- [43] Gria A, Jessell MW, Evans L, Lebensohn RA. *Geophys Res Abstracts* 2008;10:EGU2008-A-10157.
- [44] Gria A, Lebensohn RA, Jessell MW, Evans L, Bons PD. *Acta Mater*, in preparation.
- [45] Doumalin P, Bornert M, Soppa S. In: Miannay D, Coasta P, Francoise D, Pineau A, editors. *Advances in mechanical behavior, plasticity and damage*. Proceedings of EUROMAT 2000. Kidlington: Elsevier; 2000. p. 323.
- [46] Doumalin P, Bornert M, Crepin J. *Mec Ind* 2003;4:607.
- [47] Manley ME, Schulson EM. *Philos Mag* 1997;75:83.
- [48] Schulson EM. *Eng Fracture Mech* 2001;68:1839.
- [49] Barsoum MW, Radovic M, Finkel P, El-Raghy T. *Appl Phys Lett* 2001;79:479.
- [50] Acharya A, Bassani JL, Beaudoin A. *Scr Mater* 2003;48:167.
- [51] Piazzolo S, Jessell MW, Prior DJ, Bons PD. *J Microsc* 2004;213:273.
- [52] Piazzolo S, Montagnat M, Blackford J. *J Microsc* 2008;230:509.